PET of Vascular Endothelial Growth Factor Receptor Expression

Weibo Cai*[1], Kai Chen*[1], Khalid A. Mohamedali[2], Qizhen Cao[1], Sanjiv S. Gambhir[1,3], Michael G. Rosenblum[2], and Xiaoyuan Chen[1]

[1]Molecular Imaging Program at Stanford (MIPS), Department of Radiology and Bio-X Program, Stanford University School of Medicine, Stanford, California; [2]Department of Experimental Therapeutics, M.D. Anderson Cancer Center, Houston, Texas; and [3]Department of Bioengineering, Stanford University, Stanford, California

For solid tumors and metastatic lesions, tumor vascularity is a critical factor in assessing response to therapy. Here we report the first example, to our knowledge, of ^{64}Cu-labeled vascular endothelial growth factor 121 ($VEGF_{121}$) for PET of VEGF receptor (VEGFR) expression in vivo. **Methods:** $VEGF_{121}$ was conjugated with 1,4,7,10-tetraazadodecane-*N,N′,N″,N‴*-tetraacetic acid (DOTA) and then labeled with ^{64}Cu for small-animal PET of mice bearing different sized U87MG human glioblastoma xenografts. Blocking experiments and ex vivo histopathology were performed to confirm the in vivo results. **Results:** There were 4.3 ± 0.2 DOTA molecules per $VEGF_{121}$, and the VEGFR2 binding affinity of DOTA-$VEGF_{121}$ was comparable to $VEGF_{121}$. ^{64}Cu labeling of DOTA-$VEGF_{121}$ was achieved in 90 ± 10 min and the radiolabeling yield was 87.4% ± 3.2%. The specific activity of ^{64}Cu-DOTA-$VEGF_{121}$ was 3.2 ± 0.1 GBq/mg with a radiochemical purity of >98%. Small-animal PET revealed rapid, specific, and prominent uptake of ^{64}Cu-DOTA-$VEGF_{121}$ in small U87MG tumors (high VEGFR2 expression) but significantly lower and sporadic uptake in large U87MG tumors (low VEGFR2 expression). No appreciable renal clearance of ^{64}Cu-DOTA-$VEGF_{121}$ was observed, although the kidney uptake was relatively high likely due to VEGFR1 expression. Blocking experiments, immunofluorescence staining, and western blot confirmed the VEGFR specificity of ^{64}Cu-DOTA-$VEGF_{121}$. **Conclusion:** Successful demonstration of the ability of ^{64}Cu-DOTA-$VEGF_{121}$ to visualize VEGFR expression in vivo may allow for clinical translation of this radiopharmaceutical for imaging tumor angiogenesis and guiding antiangiogenic treatment, especially patient selection and treatment monitoring of VEGFR-targeted cancer therapy.

Key Words: vascular endothelial growth factor; Flk-1/KDR (vascular endothelial growth factor receptor 2); PET; tumor vasculature; ^{64}Cu

J Nucl Med 2006; 47:2048–2056

Vascular endothelial growth factor A (VEGF-A) plays a central role in both normal vascular tissue development and tumor neovascularization (*1*). VEGF-A is an endothelial cell-specific angiogenic protein expressed in various human tumors (*2*). Through alternative splicing of RNA, VEGF may exist as at least 7 different molecular isoforms, having 121, 145, 148, 165, 183, 189, or 206 amino acids (*3*). These isoforms differ not only in their molecular weight but also in their biologic properties, such as the ability to bind to cell-surface heparin sulfate proteoglycans. $VEGF_{121}$ is a soluble, nonheparin-binding variant that exists in solution as a disulfide-linked homodimer containing the full biologic and receptor-binding activity of the larger variants (*1,4*).

The angiogenic actions of VEGF are mediated primarily via two closely related endothelium-specific receptor tyrosine kinases, Flt-1 (VEGF receptor 1 [VEGFR1]) and Flk-1/KDR (VEGFR2) (*5*). Both are largely restricted to vascular endothelial cells and are overexpressed on the endothelium of tumor vasculature, yet they are almost undetectable in the vascular endothelium of adjacent normal tissues (*2*). All of the VEGF-A isoforms bind to both VEGFR1 and VEGFR2. VEGF and its receptors are overexpressed in a variety of solid tumor biopsy specimens, and overexpression of VEGFR2 or VEGF-A has been implicated as a poor prognostic marker in various clinical studies (*6–8*). Agents that prevent VEGF-A binding to its receptors (*9*), antibodies that directly block VEGFR2 (*10*), and small molecules that inhibit the kinase activity of VEGFR2 (*11,12*), and thereby block growth factor signaling, are all under active development. The contribution of VEGF-A to cancer progression has been highlighted by the recent approval of the humanized anti-VEGF monoclonal antibody bevacizumab (Avastin; Genentech) for first-line treatment (*13*). Recently, VEGFR2-targeted delivery of toxins also showed impressive antitumor vascular-ablative effects (*14,15*).

Recombinant human $VEGF_{121}$ was labeled with ^{111}In for identification of ischemic tissue in a rabbit model of unilateral hindlimb ischemia created by femoral artery excision. Only marginal difference was observed between the ischemic hindlimb and the contralateral hindlimb (*16*). ^{123}I-$VEGF_{165}$ was also reported as a potential tumor marker (*17*). Despite the high receptor affinity of this radiopharmaceutical, the biodistribution in A2508 melanoma tumor-bearing mice indicated

Received Jul. 13, 2006; revision accepted Sep. 11, 2006.

For correspondence or reprints contact: Xiaoyuan Chen, PhD, Molecular Imaging Program at Stanford (MIPS), Department of Radiology and Bio-X Program, Stanford University School of Medicine, 1201 Welch Rd., P095, Stanford, CA 94305-5484.

E-mail: shawchen@stanford.edu

*Contributed equally to this work.

low tumor-to-background ratio, most likely due to the low metabolic stability of the compound (*18*). $VEGF_{121}$ has been labeled with ^{99m}Tc through an "adapter/docking" strategy for imaging 4T1 murine mammary carcinoma tumors. Low tumor signal (~2−4 percentage injected dose per gram [%ID/g]) and poor tumor-to-background contrast were obtained (*19*). A recombinant protein composed of $VEGF_{165}$ fused through a flexible polypeptide linker $(GGGGS)_3$ to the n-lobe of human transferrin (hnTf) has also been reported for imaging tumor angiogenesis, and the tumor uptake was modest (*20*). In all of these reports, radiolabeled VEGF molecules were used for SPECT with limited success. To date, no radiolabeled VEGF has been developed for PET for any type of disease, although a few radiolabeled anti-VEGF antibodies have been reported (*21,22*). PET has several advantages over SPECT, including 10-fold greater sensitivity, and the increasing implementation of clinical PET and PET/CT scanners can facilitate the translation of novel PET radiopharmaceuticals to the clinic (*23*).

Successful development of VEGF-based PET could serve as a paradigm for assessment of cancer therapeutics targeting tumor angiogenesis. The ability to noninvasively visualize and quantify tumor VEGFR expression levels could provide new opportunities to document tumor angiogenesis status, more appropriately select patients considered for antiangiogenic treatment, and monitor antiangiogenic treatment efficacy more effectively. Herein we report, to our knowledge, the first example of ^{64}Cu (half-life, 12.7 h; 39% β^-; 17.4% β^+)-labeled $VEGF_{121}$ for PET of tumor angiogenesis and VEGFR expression.

MATERIALS AND METHODS

All commercially available chemical reagents were used without further purification. 1,4,7,10-Tetraazadodecane-*N,N′,N″,N‴*-tetraacetic acid (DOTA) was purchased from Macrocyclics, Inc. 1-Ethyl-3-[3-(dimethylamino)propyl]carbodiimide, *N*-hydroxysulfonosuccinimide, and Chelex 100 resin (50–100 mesh) were purchased from Aldrich. Water and all buffers were passed through a Chelex 100 column before use in radiolabeling procedures to ensure heavy metal–free conditions. PD-10 columns were purchased from GE Healthcare. Female athymic nude mice were supplied by Harlan at 4–5 wk of age. ^{64}Cu was obtained from the University of Wisconsin, Madison.

$VEGF_{121}$ Preparation

The gene for $VEGF_{121}$ was cloned by polymerase chain reaction from human umbilical vein endothelial cells, sequenced, and inserted into the pET-32 vector (Novagen) downstream from the cleavable His_6 tag sequence. Bacterial host cells were transformed and selected under antibiotic resistance, and positive clones were selected for optimal protein expression. Cells were lysed by sonication. The lysate was ultracentrifuged at 40,000 rpm for 90 min at 4°C. The supernatant was carefully collected, adjusted to 40 mmol/L Tris-HCl (pH 8.0) and 300 mmol/L NaCl, and run through an immobilized metal affinity column (cobalt). The resin was washed with 40 mmol/L Tris-HCl (pH 8.0), 0.3 mol/L NaCl, and 20 mmol/L imidazole buffer and eluted with buffer containing 300 mmol/L imidazole. After pooling fractions containing the His-tagged $VEGF_{121}$, the sample was dialyzed against 20 mmol/L Tris-HCl (pH 8.0) and 100 mmol/L NaCl and digested with recombinant enterokinase at room temperature to cleave the His_6 tag from $VEGF_{121}$. The enterokinase was removed by agarose-linked soybean trypsin inhibitor. The sample was then dialyzed against 20 mmol/L Tris-HCl (pH 8.0) and $VEGF_{121}$ was purified by NaCl gradient elution after binding to Q Sepharose Fast Flow resin (GE Healthcare). $VEGF_{121}$ was concentrated using Centricon 10 concentrators (Amicon, Inc.) and stored in sterile phosphate-buffered saline (PBS) at −20°C.

DOTA Conjugation and Radiolabeling

The detailed procedure for DOTA conjugation has been reported earlier (*24,25*). DOTA-$VEGF_{121}$ was purified using a PD-10 column and concentrated by Centricon filter (Ultracel YM-10; Millipore). The final concentration of DOTA-$VEGF_{121}$ was determined on the basis of ultraviolet absorbance at 280 nm using unconjugated $VEGF_{121}$ of known concentrations as the standard. $^{64}CuCl_2$ (74 MBq) was diluted in 300 μL of 0.1 mol/L sodium acetate buffer (NaOAc, pH 6.5) and added to 20 μg of DOTA-$VEGF_{121}$. The reaction mixture was incubated for 1 h at 40°C with constant shaking. ^{64}Cu-DOTA-$VEGF_{121}$ was purified using a PD-10 column with PBS as the mobile phase. The radioactive fractions containing ^{64}Cu-DOTA-$VEGF_{121}$ were collected and passed through a 0.2-μm low-protein-binding syringe filter (Nalge Nunc International) for further in vitro and in vivo experiments. ^{64}Cu-DOTA-$VEGF_{121}$ was also incubated with complete mouse serum at 37°C for up to 24 h to evaluate the stability of this radiopharmaceutical.

The average number of DOTA chelators per $VEGF_{121}$ was determined using a previously reported procedure with slight modifications (*26*). Briefly, 5 μg of DOTA-$VEGF_{121}$ in 100 μL 0.1N NaOAc buffer were added to a defined amount of carrier-added $^{64}CuCl_2$ solution. The number of DOTA molecules per $VEGF_{121}$ was calculated using the following equation:

$$\text{Number of DOTA molecules per VEGF}_{121} = \text{moles of } (Cu^{2+}) \times \text{yield}/\text{moles of } (\text{DOTA-VEGF}_{121}).$$

The results are expressed as mean ± SD ($n = 3$).

Cell Lines and Animal Model

The U87MG human glioblastoma cell line was obtained from the American Type Culture Collection and cultured under standard conditions (*27,28*). Porcine aortic endothelial cells that express human KDR (PAE/KDR) were cultured in Ham's F-12 medium containing 10% fetal calf serum (Sigma). Animal procedures were performed according to a protocol approved by the Stanford University Institutional Animal Care and Use Committee. The U87MG tumor model was generated by subcutaneous injection of 5×10^6 cells in 50 μL PBS into the front leg of the mice. The mice were subjected to microPET studies when the tumor volume reached about 60 mm^3 (small tumor, 1–2 wk after inoculation) or 1,200 mm^3 (large tumor, 4 wk after inoculation).

Cell-Binding Assay and Functional Assay

The detailed procedure for the cell-binding assay has been reported earlier (*29,30*). Receptor-binding affinity of $VEGF_{121}$ and

DOTA-$VEGF_{121}$ was analyzed by PAE/KDR cell-binding assay using ^{125}I-$VEGF_{165}$ as the radioligand. To determine the functional activity of DOTA-$VEGF_{121}$, PAE/KDR cells were stimulated by serial concentrations of $VEGF_{121}$ or DOTA-$VEGF_{121}$ for 5 min, and the cell lysates were immunoblotted by antiphophorylated VEGFR2 antibody (Abcam Inc.).

MicroPET Studies

PET of tumor-bearing mice was performed on a microPET R4 rodent model scanner (Siemens Medical Solutions USA, Inc.) as described earlier (*31,32*). Each mouse was injected with about 5–10 MBq of ^{64}Cu-DOTA-$VEGF_{121}$ (~2–4 μg of $VEGF_{121}$) via tail vein. For each microPET scan, 3-dimensional region of interests (ROIs) were drawn over the tumor, liver, kidneys, and muscle on decay-corrected whole-body coronal images. The average radioactivity concentration within a tumor or an organ was obtained from mean pixel values within the ROI volume, which were converted to counts per milliliter per minute by using a conversion factor. Assuming a tissue density of 1 g/mL, the counts per milliliter per minute were converted to counts per gram per minute and then divided by the injected dose (ID) to obtain an imaging ROI-derived %ID/g. Mice bearing small U87MG tumors were also imaged using ^{64}Cu-DOTA-$VEGF_{121}$ injected 30 min after injection of 100 μg of $VEGF_{121}$ ($n = 3$). Nine mice were used for this study: 3 small tumor-bearing mice, 3 large tumor-bearing mice, and 3 mice for blocking and biodistribution studies.

Radiation Dosimetry Extrapolation to Humans

Estimated human dosimetry was calculated from microPET results on Sprague–Dawley female rats (Harlan) injected with about 37 MBq of ^{64}Cu-DOTA-$VEGF_{121}$ ($n = 3$), assuming that the biodistribution of the radiopharmaceutical in rats is the same as in adult humans. The rats were scanned at 2 bed positions to cover the whole body, and ROI analysis was performed on major organs. Time–activity curves were generated from the mean values obtained in rats for each organ of interest. We then calculated source organ residence times for the human model by integrating a monoexponential fit to the experimental biodistribution data for major organs (blood, liver, kidneys, and muscle) and the whole body. The source organ residence times obtained forthwith were used with a standard quantitation platform, Organ Level Internal Dose Assessment (OLINDA; Vanderbilt University) (*33*).

Western Blot

U87MG tumor tissue protein was extracted using T-PER tissue protein extraction buffer (Pierce Biotechnology, Inc.) and the concentration was determined using a MicroBCA Protein Assay kit (Pierce Biotechnology, Inc.). After sodium dodecyl sulfate polyacrylamide gel electrophoresis (SDS-PAGE) separation of 100 μg of total protein, it was transferred to a polyvinylidene fluoride membrane (Invitrogen Corp.) and incubated at room temperature with 5% nonfat milk blocking buffer. The blots were then incubated overnight at 4°C with rabbit anti-VEGFR2 primary antibody (Lab Vision Corp.) followed by incubation at room temperature for 1 h with horseradish peroxidase–conjugated antirabbit secondary antibody (GE Healthcare). Tubulin was used as the loading control, and the bands were detected using the electrochemoluminescent Western Blotting Detection system (GE Healthcare).

Immunofluorescence Staining

U87MG tumor and kidney frozen tissue slices (5-μm thickness) were fixed with cold acetone for 10 min and dried in air for 30 min. The slices were rinsed with PBS for 2 min and blocked with 10% donkey serum for 30 min at room temperature. The slices were then incubated with rat antimouse VEGFR2 antibody overnight at 4°C and visualized using Cy3-conjugated donkey antirat secondary antibody (1:200; Jackson ImmunoResearch Laboratories, Inc.). For VEGFR1 staining, the tissue slices were incubated with rabbit antimouse VEGFR1 antibody (1:50; Lab Vision Corp.) at room temperature for 1 h and visualized with Cy3-conjugated donkey antirabbit secondary antibody (1:200; Jackson ImmunoResearch Laboratories, Inc.). For CD31 staining, the slices were incubated with rat antimouse CD31 antibody (1:100; BD Biosciences) at room temperature for 1 h and visualized with Cy3-conjugated donkey antirat secondary antibody (1:200; Jackson ImmunoResearch Laboratories, Inc.).

After CD31 staining, 7 random views in both the center and the periphery of the tumor slices were selected for microvessel density (MVD) analysis using an observer-set threshold to distinguish vascular elements from surrounding tissue parenchyma. The vessel that contains branching points was counted as a single vessel. The number of vessels counted was divided by the field of view to yield the MVD, as vessels/mm^2.

Statistical Analysis

Quantitative data were expressed as mean ± SD. Means were compared using 1-way ANOVA and the Student *t* test. *P* values < 0.05 were considered statistically significant.

RESULTS

Receptor-Binding Assay and Functional Activity of DOTA-$VEGF_{121}$

The binding of $VEGF_{121}$ and DOTA-$VEGF_{121}$ to endothelial cells expressing VEGFR2 was assessed using ^{125}I-$VEGF_{165}$ as the radioligand. The 50% inhibitory concentration (IC_{50}) values were 1.02 nmol/L and 1.66 nmol/L for $VEGF_{121}$ and DOTA-$VEGF_{121}$, respectively (Fig. 1A). The minimal difference in VEGFR2 binding affinity between $VEGF_{121}$ and DOTA-$VEGF_{121}$ suggested that the lysine residues or N-terminal amine groups used for DOTA conjugation may not be located at the VEGFR2 binding domain. DOTA conjugation of $VEGF_{121}$ resulted in decreased functional activity (Fig. 1B). However, full functional activity is not required for imaging applications.

Radiolabeling of DOTA-$VEGF_{121}$

^{64}Cu labeling, including the final purification, of DOTA-$VEGF_{121}$ took 90 ± 10 min ($n = 5$), and the radiolabeling yield was 87.4% ± 3.2% (based on 37 MBq of ^{64}Cu per 10 μg of DOTA-$VEGF_{121}$; $n = 5$). The specific activity of ^{64}Cu-DOTA-$VEGF_{121}$ was 3.2 ± 0.1 GBq/mg, with a radiochemical purity of >98%. The number of DOTA molecules per $VEGF_{121}$ molecule was determined to be 4.3 ± 0.2 ($n = 3$). No significant metabolite peak was observed on radio–high-performance liquid chromatography when ^{64}Cu-DOTA-$VEGF_{121}$ was incubated with mouse serum at 37°C for up to 24 h, indicating that the radiopharmaceutical is stable in mouse serum.

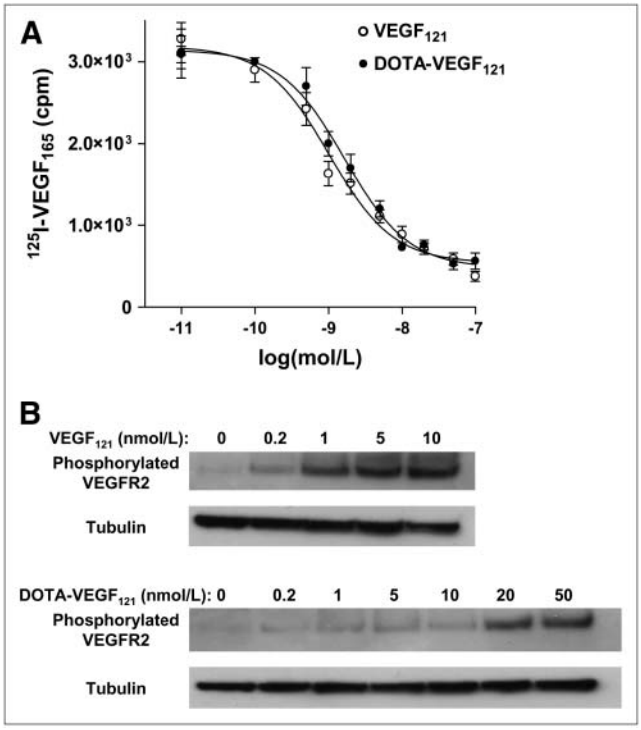

FIGURE 1. Cell-binding assay and functional assay. (A) Cell-binding assay of $VEGF_{121}$ and DOTA-$VEGF_{121}$ using PAE/KDR cells. IC_{50} values are 1.02 and 1.66 nmol/L for $VEGF_{121}$ and DOTA-$VEGF_{121}$, respectively. (B) Functional assay of $VEGF_{121}$ and DOTA-$VEGF_{121}$. Tubulin was used as loading control.

MicroPET of ^{64}Cu-DOTA-$VEGF_{121}$ in U87MG Tumor-Bearing Mice

Mice bearing small (tumor volume: 64.9 ± 24.6 mm^3, $n = 3$; high VEGFR expression) and large (tumor volume: 1,164.3 ± 179.6 mm^3, $n = 3$; low VEGFR expression) U87MG tumors were subjected to microPET scans at various time points after injection of ^{64}Cu-DOTA-$VEGF_{121}$. The coronal slices that contain the tumor are shown in Figure 2A. The uptake of ^{64}Cu-DOTA-$VEGF_{121}$ into small tumors was rapid and high, reaching 14.9 ± 0.7, 16.3 ± 0.7, 16.3 ± 0.6, and 15.1 ± 0.8 %ID/g at 2, 4, 16, and 23 h after injection, respectively. As early as 1 h after injection, the tumor was clearly visible (data not shown). The accumulation of ^{64}Cu-DOTA-$VEGF_{121}$ in the large tumor was at a very low level at all time points examined, with the uptake at the peripheral region (~3–4 %ID/g) slightly higher than at the necrotic center of the tumor (~1–2 %ID/g). The ^{64}Cu-DOTA-$VEGF_{121}$ uptake was significantly different between the small tumors and the large tumors at all time points examined ($P < 0.01$, Fig. 3A).

^{64}Cu-DOTA-$VEGF_{121}$ exhibited high uptake in the kidneys and liver at early time points (33.0 ± 13.5 and 17.1 ± 3.2 %ID/g at 2 h after injection, respectively; $n = 6$, 3 small tumor-bearing mice and 3 large tumor-bearing mice). The uptake in most other organs was at a very low level. The uptake of ^{64}Cu-DOTA-$VEGF_{121}$ in both the kidneys and the liver dropped steadily over time (Fig. 3B). For the kidneys, the uptake was 33.0 ± 13.5, 21.3 ± 7.3, and 13.5 ± 3.5 %ID/g at 2, 23, and 47 h after injection, respectively. Although the kidney uptake was high, there was no appreciable activity accumulation in the urinary bladder, suggesting a very slow renal clearance rate of ^{64}Cu-DOTA-$VEGF_{121}$.

Blocking and Biodistribution Studies

To test the VEGFR specificity of ^{64}Cu-DOTA-$VEGF_{121}$ in vivo, blocking experiments were performed, in which 100 μg $VEGF_{121}$ were injected into small U87MG tumor-bearing mice (tumor volume, 61.3 ± 10.6 mm^3, $n = 3$) 30 min before administration of ^{64}Cu-DOTA-$VEGF_{121}$. As can be seen from both the coronal slices (Fig. 2A) and the 2-dimensional whole-body projection at 16 h after injection (Fig. 2B), the small U87MG tumor uptake is clearly lower compared with that of those mice without $VEGF_{121}$ blocking. Although 100 μg of $VEGF_{121}$ (~4 mg/kg) was unable to completely block the tumor uptake of ^{64}Cu-DOTA-$VEGF_{121}$, the activity accumulation in the tumor (9.2 ± 1.7, 10.5 ± 0.6, 11.4 ± 0.2, and 10.3 ± 0.8 %ID/g at 2, 4, 16, and 23 h after injection, respectively) was significantly lower at all time points examined compared with that of the control mice ($P < 0.05$; Fig. 3C). The kidney uptake of ^{64}Cu-DOTA-$VEGF_{121}$ was also lower in the mice injected with $VEGF_{121}$. However, statistical significance was achieved only at 23 h after injection (Fig. 3D), due to the large variance in kidney uptake between individual animals and the insufficient blocking dose of $VEGF_{121}$. The variance in kidney uptake of ^{64}Cu-DOTA-$VEGF_{121}$ between each individual animal was not fully understood. Successful partial blocking of the small U87MG tumor and the kidney uptake with a limited dose of $VEGF_{121}$ demonstrated the VEGFR specificity of ^{64}Cu-DOTA-$VEGF_{121}$ in vivo.

After the microPET scans at 23 h after injection, the mice were immediately sacrificed and biodistribution studies were performed (Fig. 3E). When comparing the quantification results obtained from biodistribution studies and PET scans, there was no significant difference between the liver, tumor, and muscle ($P > 0.05$; Fig. 3F), suggesting that quantification of noninvasive microPET scans is a true reflection of the biodistribution of ^{64}Cu-DOTA-$VEGF_{121}$ in these organs. The difference in kidney uptake between the 2 studies was likely due to the heterogeneity of ^{64}Cu-DOTA-$VEGF_{121}$ uptake in the kidney and the difficulty in ROI analysis because of its irregular shape.

Immunofluorescence Staining and Western Blot

After decay of most of the radioactivity in the microPET studies, the mice were sacrificed and the frozen tumor slices were stained for CD31, VEGFR1, and VEGFR2. As can be seen in Figure 4, VEGFR1 expression was low in both small and large U87MG tumors. VEGFR1 expression is known to be expressed on endothelial cells of preglomerular vessels, glomeruli, and postglomerular vessels in the kidneys, which is most likely responsible for the observed high kidney uptake of ^{64}Cu-DOTA-$VEGF_{121}$. Small U87MG

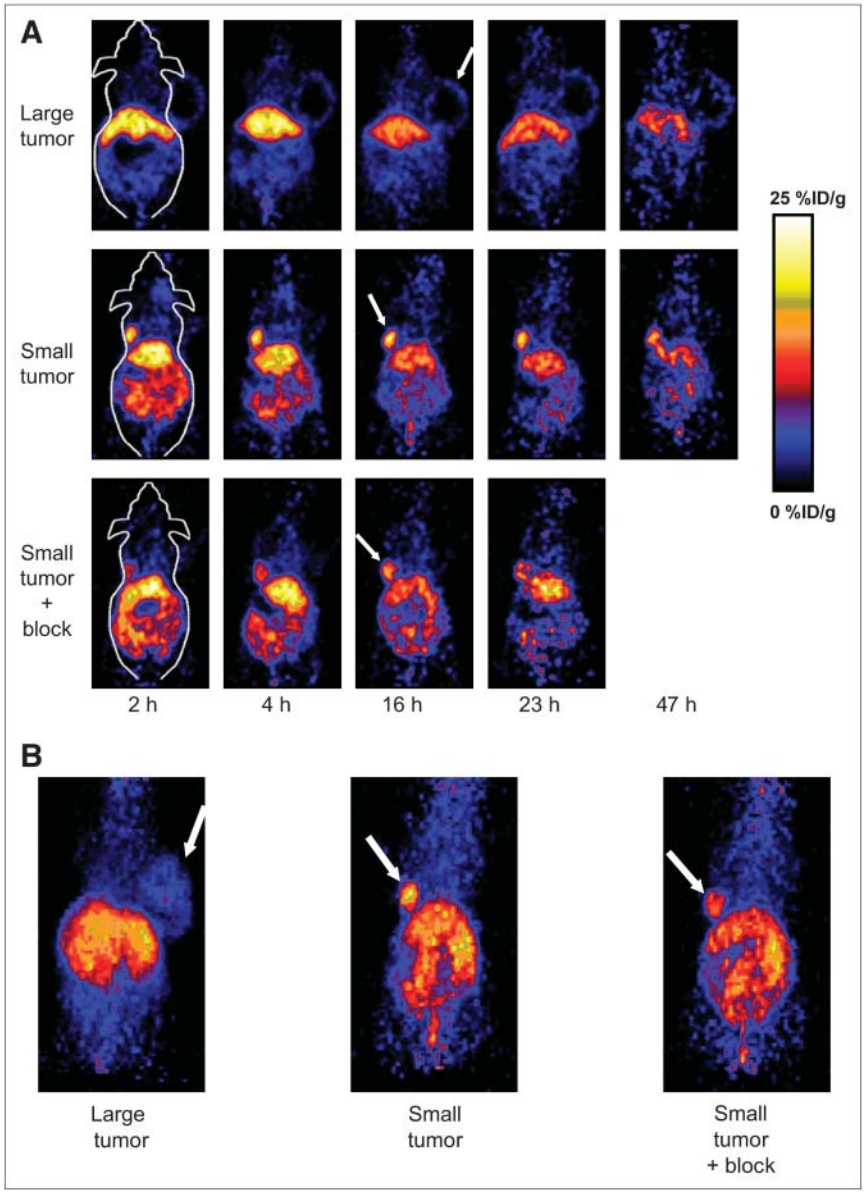

FIGURE 2. MicroPET of ^{64}Cu-DOTA-VEGF$_{121}$ in U87MG tumor-bearing mice. (A) Serial microPET scans of large and small U87MG tumor-bearing mice injected intravenously with 5–10 MBq of ^{64}Cu-DOTA-VEGF$_{121}$ (~2–4 μg of VEGF$_{121}$). Mice injected with ^{64}Cu-DOTA-VEGF$_{121}$ 30 min after injection of 100 μg VEGF$_{121}$ are also shown (denoted as "Small tumor + block"). (B) Two-dimensional whole-body projection of the 3 mice shown in A at 16 h after injection of ^{64}Cu-DOTA-VEGF$_{121}$. Tumors are indicated by arrows.

tumors had high VEGFR2 expression, whereas large tumors demonstrated very low VEGFR2 expression, resulting in high ^{64}Cu-DOTA-VEGF$_{121}$ uptake in small U87MG tumors but very low uptake in large tumors. There was also a measurable level of VEGFR2 in the kidneys, primarily on the small vessels but not on the large, mature vessels. CD31 staining indicated much higher vascular density in the small U87MG tumor than in the large tumor. The vessels in the small tumor were mostly of regular shape, whereas the vessels in the large U87MG tumor had much larger diameter and the shapes were more irregular. Costaining of VEGFR2 and CD31 was unsuccessful. However, visual examination of CD31 and VEGFR2 staining of different slices in the same tumor suggests that VEGFR2 and CD31 are colocalized on the newly developed tumor vessels. MVD analysis revealed that the small U87MG tumor has a significantly higher vessel density (96 ± 19 vessels/mm^2) than the large tumor (20 ± 9 vessels/mm^2; $P < 0.01$, Fig. 5A). Western blot also showed a higher VEGFR2 protein level in the small U87MG tumor than in the large tumor (Fig. 5B). Because of the low expression level of VEGFR1 in both the small and the large U87MG tumors, a western blot of VEGFR1 was not obtained. The good correlation of ex vivo results with in vivo microPET indicates that noninvasive microPET using ^{64}Cu-DOTA-VEGF$_{121}$ can reflect the VEGFR expression level in vivo.

Radiation Dosimetry

Human absorbed doses to normal organs from ^{64}Cu-DOTA-VEGF$_{121}$ were estimated from microPET quantification data in female Sprague–Dawley rats, assuming that the biodistribution and pharmacokinetics of ^{64}Cu-DOTA-VEGF$_{121}$ in rats and adult human are the same, and the results are presented in Table 1. The ^{64}Cu-DOTA-VEGF$_{121}$

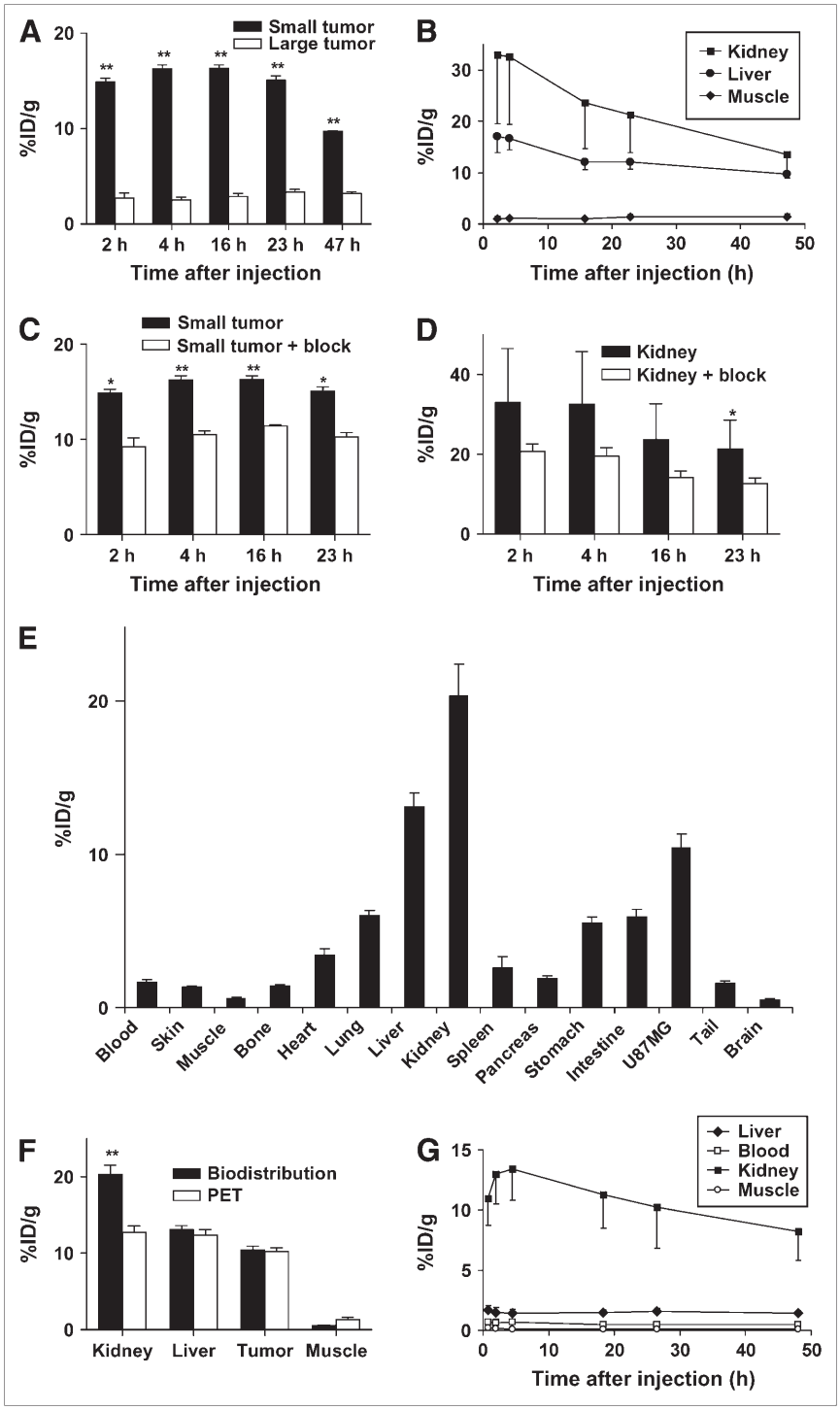

FIGURE 3. MicroPET and biodistribution results. (A) Comparison of ^{64}Cu-DOTA-VEGF$_{121}$ uptake in small and large U87MG tumors (3 mice per group). (B) Time–activity curves of ^{64}Cu-DOTA-VEGF$_{121}$ uptake in the kidney, liver, and muscle (n = 6). (C) Comparison of ^{64}Cu-DOTA-VEGF$_{121}$ uptake in small U87MG tumors with those injected previously with 100 μg of VEGF$_{121}$ (3 mice per group). (D) Comparison of ^{64}Cu-DOTA-VEGF$_{121}$ uptake in kidneys (n = 6) with those injected previously with 100 μg of VEGF$_{121}$ (n = 3). (E) Biodistribution at 23 h after injection of ^{64}Cu-DOTA-VEGF$_{121}$ in mice injected previously with 100 μg of VEGF$_{121}$ (n = 3). (F) Comparison of quantification results obtained from biodistribution and microPET studies (n = 3). (G) Time–activity curves of liver, blood, kidney, and muscle in Sprague–Dawley rats injected with ^{64}Cu-DOTA-VEGF$_{121}$ (n = 3). *$P < 0.05$; **$P < 0.01$.

uptake of different organs in rats was similar to that of mice (Fig. 3G). Except for the blood, liver, and kidneys, all other organs exhibited very low level of ^{64}Cu-DOTA-VEGF$_{121}$ uptake at all time points examined. The radiopharmaceutical was excreted primarily via the hepatic pathway. No appreciable activity was observed in the urinary bladder at all time points examined, suggesting that ^{64}Cu-DOTA-VEGF$_{121}$ also has a very slow renal clearance in rats. The highest radiation-absorbed dose is to the kidneys (1.05 ± 0.27 mGy/MBq). Except for the kidneys and the liver (0.12 ± 0.02 mGy/MBq), all other organs have a very low level of radiation-absorbed doses. The whole-body absorbed dose was found to be 0.05 ± 0.01 mGy/MBq administered. Although the dose-limiting organ is the kidneys, the relatively low radiation dose will not likely cause any adverse effect, as ^{64}Cu-DOTA-VEGF$_{121}$ will be used only for

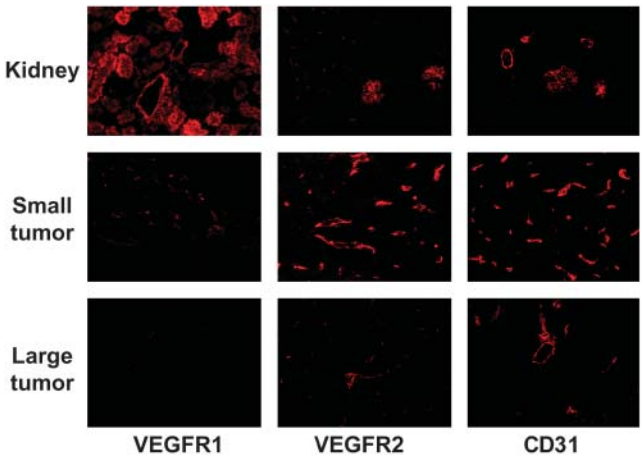

FIGURE 4. Immunofluorescence staining of VEGFR1, VEGFR2, and CD31 for kidney, small U87MG tumor, and large U87MG tumor. For VEGFR1 staining, frozen tissue slices (5-μm thick) were stained with a rabbit antimouse VEGFR1 primary antibody and a Cy3-conjugated donkey antirabbit secondary antibody. For VEGFR2 staining, tissue slices were stained with a rat antimouse VEGFR2 primary antibody and a Cy3-conjugated donkey antirat secondary antibody. For CD31 staining, slices were stained with a rat antimouse CD31 primary antibody and a Cy3-conjugated donkey antirat secondary antibody.

imaging application, where limited radioactivity (~200–400 MBq) will be injected in patients.

TABLE 1
Estimated Radiation-Absorbed Doses to Adult Human After Intravenous Injection of ^{64}Cu-DOTA-VEGF$_{121}$ Based on microPET Imaging Data Obtained in Female Sprague–Dawley Rats (n = 3)

Organ	mGy/MBq (SD)	rad/mCi (SD)
Adrenals	3.62E−02 (1.87E−03)	1.34E−01 (6.56E−03)
Brain	1.61E−02 (1.13E−03)	5.96E−02 (4.08E−03)
Breasts	1.68E−02 (9.64E−04)	6.22E−02 (3.76E−03)
Gallbladder	3.43E−02 (8.02E−04)	1.27E−01 (3.00E−03)
LLI wall	2.02E−02 (1.04E−03)	7.49E−02 (3.93E−03)
Stomach	2.48E−02 (3.06E−04)	8.95E−02 (1.79E−03)
ULI wall	2.45E−02 (5.20E−04)	9.06E−02 (1.82E−03)
Heart	2.20E−02 (1.07E−03)	8.14E−02 (3.93E−03)
Kidneys	1.05E+00 (2.72E−01)	3.87E+00 (1.01E+00)
Liver	1.17E−01 (1.88E−02)	4.33E−01 (6.89E−02)
Lungs	2.03E−02 (1.03E−03)	7.51E−02 (3.73E−03)
Muscle	1.96E−02 (7.51E−04)	7.28E−02 (2.77E−03)
Ovaries	2.12E−02 (9.81E−04)	7.84E−02 (3.72E−03)
Pancreas	3.26E−02 (7.09E−04)	1.21E−01 (2.52E−03)
Skin	1.63E−02 (8.39E−04)	6.05E−02 (3.09E−03)
Spleen	8.45E−02 (9.79E−03)	3.13E−01 (3.63E−02)
Testes	1.72E−02 (1.16E−03)	6.35E−02 (4.19E−03)
Thymus	1.86E−02 (1.14E−03)	6.87E−02 (4.19E−03)
Thyroid	1.77E−02 (1.18E−03)	6.56E−02 (4.37E−03)
Urinary	1.95E−02 (1.18E−03)	7.22E−02 (4.39E−03)
Uterus	2.11E−02 (1.04E−03)	7.82E−02 (3.81E−03)
Effective dose	5.03E−02 (5.50E−03)	1.86E−01 (2.07E−02)

LLI = lower large intestine; ULI = upper large intestine.

DISCUSSION

This study demonstrated that ^{64}Cu-labeled VEGF$_{121}$ exhibits strong and specific VEGFR-binding affinity both in vitro and in vivo. Food and Drug Administration approval of anti-VEGF antibody bevacizumab and the fact that many other antibody and small molecule inhibitors against VEGFR2 are currently in advanced clinical trials confirm the validity and importance of VEGF/VEGFR2 signaling in anticancer therapy (*10–12*). PET using radiolabeled VEGF$_{121}$ is critical in early and sensitive lesion detection, in patient selection for clinical trials based on in vivo VEGFR expression quantification, in better treatment monitoring and dose optimization based on noninvasive detection of early response to VEGF- or VEGFR-targeted therapy, and in elucidating the mechanisms of treatment efficacy underlying VEGF/VEGFR signaling.

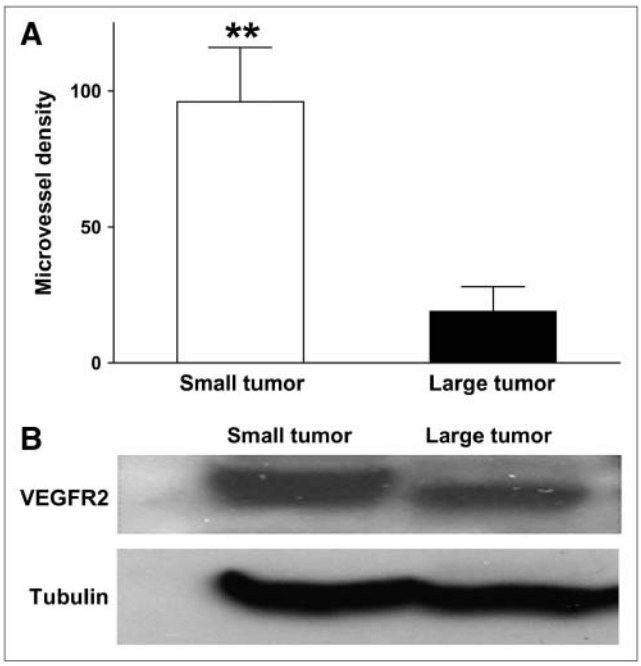

FIGURE 5. MVD analysis and western blot. (A) MVD analysis of small and large U87MG tumor. $^{**}P < 0.01$. (B) Western blot of VEGFR2 in small and large U87MG tumor. Tubulin was used as loading control.

It is well accepted that tumor angiogenesis occurs when the tumor reaches a certain size (usually 1–2 mm in diameter), as new blood vessel formation is needed to supply oxygen and nutrients to cancer cells and to remove waste (*34*). VEGF-A and its receptors are the best-characterized signaling pathway in developmental angiogenesis as well as tumor angiogenesis (*2*). VEGFR2 appears to be the most important receptor in VEGF-induced mitogenesis, angiogenesis, and permeability increase, whereas the role of VEGFR1 in endothelial cell function is less clear (*1*). During the exponential growth stage, VEGFR expression is highly upregulated on the newly developed tumor vasculature.

Being the naturally existing VEGFR ligand, $VEGF_{121}$ offers several advantages over the synthetic small-molecule VEGFR ligands or anti-VEGFR antibodies. It has much higher binding affinity to VEGFR (nanomolar range) than reported peptidic VEGFR inhibitors (submicromolar to micromolar range) (*35,36*). Comparing with antibody-based radiopharmaceuticals, $VEGF_{121}$ clears much faster from the blood pool and the nontargeting organs because of its smaller size (25 kDa for the dimeric form of $VEGF_{121}$). In this proof-of-principle study, we chose two different sizes of the same tumor type, hypothesizing that the small tumors have higher VEGFR expression than the large tumors.

Indeed, in the small U87MG tumor, where the diameter is about 4–6 mm, the tumor is at an exponential growth stage. Both immunofluorescence staining (VEGFR1, VEGFR2, and CD31; Fig. 4) and western blot (Fig. 5B) demonstrated that there is a high level of VEGFR2 expression in the tumor. For the large tumor, where the tumor diameter is about 10–15 mm, the tumor vessels are primarily mature (much larger diameter compared with the vessels in the small tumor, and the vessel density is also much lower), and both VEGFR1 and VEGFR2 expression are quite low, as confirmed by ex vivo immunofluorescence staining and western blot. The ex vivo results supported the in vivo PET findings, where the small tumors have much higher ^{64}Cu-DOTA-$VEGF_{121}$ uptake (~15 %ID/g) than that in the large tumors (~2–3 %ID/g). PET of other less vascularized tumors (e.g., MDA-MB-435 breast cancer, where the vessel density is quite low when the tumor reaches a certain size) also exhibited very low ^{64}Cu-DOTA-$VEGF_{121}$ uptake (data not shown). Tiny (<2 mm in diameter) and medium-size (8–10 mm in diameter) U87MG tumors had a very low (<3 %ID/g) and an intermediate level (5–8 %ID/g) of ^{64}Cu-DOTA-$VEGF_{121}$ uptake, respectively (data not shown). These results suggest that the time window of high VEGFR expression is quite narrow. In the clinical setting, the right timing is critical for VEGFR-targeted cancer therapy. PET using ^{64}Cu-DOTA-$VEGF_{121}$ can play a very important role in determining whether, and when, to start the VEGFR-targeted cancer therapy, as it can provide a straightforward and convenient way to monitor VEGFR expression level in vivo.

In addition to immunofluorescence staining and western blot analysis, FACS sorting of tumor cells may be another method to quantify VEGFR2 expression. Tumor cells can be harvested and stained for CD31 or VEGFR1/VEGFR2. Florescence-activated cell sorter analysis can then be performed to evaluate the VEGFR1/VEGFR2 expression level on endothelial cells. Other microvessel markers such as CD105 may also be used to correlate VEGFR expression and MVD in future studies (*37*). VEGFR2-specific ligand can be developed in the future. It may offer a certain advantage over $VEGF_{121}$-based radiopharmaceuticals, such as lower renal uptake ($VEGF_{121}$ binds both VEGFR1 and VEGFR2 and kidney has high VEGFR1 expression). A certain level of VEGFR2 expression in the kidney was also observed in this study (Fig. 4). Comparison of the CD31 and VEGFR2 staining of the kidney slices showed that the VEGFR2 expression is localized primarily to the glomerulus but not on the big vessels (e.g., intralobular vein or the efferent arteriole), which is expected as VEGFR2 is expressed primarily on microvessels. Peptidic VEGFR antagonists that can be labeled with ^{18}F (more readily available than ^{64}Cu) may also be tested, and it can allow for high throughput, as usually 1–2 h after injection is sufficient for a peptide-based radiopharmaceutical to clear from the nontargeted organs and give high-contrast PET images.

Endogenous VEGF isoforms may also compete with ^{64}Cu-DOTA-$VEGF_{121}$ in VEGFR binding. However, the intact VEGFR-binding potency of DOTA-$VEGF_{121}$ and the fact that the endogenous VEGF concentration is far from saturating the VEGFR resulted in prominent ^{64}Cu-DOTA-$VEGF_{121}$ uptake in the high VEGFR-expressing small U87MG tumors. Although the functional activity of DOTA-$VEGF_{121}$ is significantly lower than that of $VEGF_{121}$, this is not a concern for imaging applications. Serial microPET of ^{64}Cu-DOTA-$VEGF_{121}$ indicated that ^{64}Cu is the optimal isotope for $VEGF_{121}$-based radiopharmaceuticals, as the half-life of ^{64}Cu (12.7 h) is well suited for the time frame needed to follow the radiopharmaceutical uptake and clearance (48 h in this study, slightly less than 4 half-lives of ^{64}Cu). Although not evaluated, blood flow (related to microvessel density) may also contribute to a certain extent to the higher uptake of radioactivity in the small U87MG tumors than in the large tumors.

CONCLUSION

We report herein, to our knowledge, the first example of ^{64}Cu-labeled $VEGF_{121}$ for PET of tumor VEGFR expression. MicroPET revealed rapid and high ^{64}Cu-DOTA-$VEGF_{121}$ uptake in small U87MG tumors but very low uptake in large tumors, corresponding with the VEGFR2 expression level in vivo. VEGFR specificity in vivo was confirmed by blocking experiments and ex vivo studies. The success of VEGFR-specific tumor imaging using ^{64}Cu-DOTA-$VEGF_{121}$ may be translated into the clinic to characterize the pharmacokinetics, tumor-targeting efficacy, dose optimization, and dose interval of VEGF- or VEGFR-targeted cancer therapeutics. It may also significantly aid in patient stratification and treatment monitoring of VEGFR-targeted cancer therapy.

ACKNOWLEDGMENTS

We thank Dr. Zi-bo Li, Andrew R. Hsu, and Lina He for their excellent technical support and the cyclotron team at the University of Wisconsin, Madison, for ^{64}Cu production. We also thank Dr. Philip E. Thorpe and Dr. Sophia Ran at UT Southwestern Medical Center, Dallas, for providing the antimouse VEGFR2 primary antibody. This work was funded by National Institute of Biomedical Imaging and

Bioengineering grant R21 EB001785, National Cancer Institute (NCI) grant R21 CA102123, NCI In Vivo Cellular Molecular Imaging Center grant P50 CA114747, NCI Small Animal Imaging Resource Program grant R24 CA93862, NCI Centers of Cancer Nanotechnology Excellence grant 1U54CA119367-01, Department of Defense (DOD) Breast Cancer Research Program IDEA award W81XWH-04-1-0697, DOD Ovarian Cancer Research Program award OC050120, DOD Prostate Cancer Research Program New Investigator award DAMD17-03-1-0143, the Benedict Cassen Postdoctoral Fellowship from the Education and Research Foundation for the Society of Nuclear Medicine, and the Clayton Foundation for Research.

REFERENCES

1. Ferrara N. Vascular endothelial growth factor: basic science and clinical progress. *Endocr Rev.* 2004;25:581–611.
2. Ferrara N. The role of VEGF in the regulation of physiological and pathological angiogenesis. *EXS.* 2005;94:209–231.
3. Renner W, Pilger E. Simultaneous *in vivo* quantitation of vascular endothelial growth factor mRNA splice variants. *J Vasc Res.* 1999;36:133–138.
4. Cohen T, Gitay-Goren H, Sharon R, et al. $VEGF_{121}$, a vascular endothelial growth factor (VEGF) isoform lacking heparin binding ability, requires cell-surface heparan sulfates for efficient binding to the VEGF receptors of human melanoma cells. *J Biol Chem.* 1995;270:11322–11326.
5. Sato Y, Kanno S, Oda N, et al. Properties of two VEGF receptors, Flt-1 and KDR, in signal transduction. *Ann N Y Acad Sci.* 2000;902:201–205.
6. Tang RF, Itakura J, Aikawa T, et al. Overexpression of lymphangiogenic growth factor VEGF-C in human pancreatic cancer. *Pancreas.* 2001;22:285–292.
7. Ryden L, Linderholm B, Nielsen NH, Emdin S, Jonsson PE, Landberg G. Tumor specific VEGF-A and VEGFR2/KDR protein are co-expressed in breast cancer. *Breast Cancer Res Treat.* 2003;82:147–154.
8. Decaussin M, Sartelet H, Robert C, et al. Expression of vascular endothelial growth factor (VEGF) and its two receptors (VEGF-R1-Flt1 and VEGF-R2-Flk1/KDR) in non-small cell lung carcinomas (NSCLCs): correlation with angiogenesis and survival. *J Pathol.* 1999;188:369–377.
9. Sun J, Wang DA, Jain RK, et al. Inhibiting angiogenesis and tumorigenesis by a synthetic molecule that blocks binding of both VEGF and PDGF to their receptors. *Oncogene.* 2005;24:4701–4709.
10. Prewett M, Huber J, Li Y, et al. Antivascular endothelial growth factor receptor (fetal liver kinase 1) monoclonal antibody inhibits tumor angiogenesis and growth of several mouse and human tumors. *Cancer Res.* 1999;59:5209–5218.
11. Wood JM, Bold G, Buchdunger E, et al. PTK787/ZK 222584, a novel and potent inhibitor of vascular endothelial growth factor receptor tyrosine kinases, impairs vascular endothelial growth factor-induced responses and tumor growth after oral administration. *Cancer Res.* 2000;60:2178–2189.
12. Wedge SR, Ogilvie DJ, Dukes M, et al. ZD4190: an orally active inhibitor of vascular endothelial growth factor signaling with broad-spectrum antitumor efficacy. *Cancer Res.* 2000;60:970–975.
13. Middleton G, Lapka DV. Bevacizumab (Avastin). *Clin J Oncol Nurs.* 2004;8:666–669.
14. Backer MV, Backer JM. Targeting endothelial cells overexpressing VEGFR-2: selective toxicity of Shiga-like toxin-VEGF fusion proteins. *Bioconjug Chem.* 2001;12:1066–1073.
15. Liu Y, Cheung LH, Thorpe P, Rosenblum MG. Mechanistic studies of a novel human fusion toxin composed of vascular endothelial growth factor (VEGF)121 and the serine protease granzyme B: directed apoptotic events in vascular endothelial cells. *Mol Cancer Ther.* 2003;2:949–959.
16. Lu E, Wagner WR, Schellenberger U, et al. Targeted *in vivo* labeling of receptors for vascular endothelial growth factor: approach to identification of ischemic tissue. *Circulation.* 2003;108:97–103.
17. Li S, Peck-Radosavljevic M, Kienast O, et al. Iodine-123-vascular endothelial growth factor-165 (^{123}I-$VEGF_{165}$): biodistribution, safety and radiation dosimetry in patients with pancreatic carcinoma. *Q J Nucl Med Mol Imaging.* 2004;48:198–206.
18. Cornelissen B, Oltenfreiter R, Kersemans V, et al. *In vitro* and *in vivo* evaluation of [^{123}I]-$VEGF_{165}$ as a potential tumor marker. *Nucl Med Biol.* 2005;32:431–436.
19. Blankenberg FG, Mandl S, Cao YA, et al. Tumor imaging using a standardized radiolabeled adapter protein docked to vascular endothelial growth factor. *J Nucl Med.* 2004;45:1373–1380.
20. Chan C, Sandhu J, Guha A, et al. A human transferrin-vascular endothelial growth factor (hnTf-VEGF) fusion protein containing an integrated binding site for ^{111}In for imaging tumor angiogenesis. *J Nucl Med.* 2005;46:1745–1752.
21. Collingridge DR, Carroll VA, Glaser M, et al. The development of [^{124}I]iodinated-VG76e: a novel tracer for imaging vascular endothelial growth factor *in vivo* using positron emission tomography. *Cancer Res.* 2002;62:5912–5919.
22. Jayson GC, Zweit J, Jackson A, et al. Molecular imaging and biological evaluation of HuMV833 anti-VEGF antibody: implications for trial design of antiangiogenic antibodies. *J Natl Cancer Inst.* 2002;94:1484–1493.
23. Gambhir SS. Molecular imaging of cancer with positron emission tomography. *Nat Rev Cancer.* 2002;2:683–693.
24. Wu Y, Zhang X, Xiong Z, et al. microPET imaging of glioma integrin $\alpha_v\beta_3$ expression using ^{64}Cu-labeled tetrameric RGD peptide. *J Nucl Med.* 2005;46:1707–1718.
25. Cai W, Wu Y, Chen K, Cao Q, Tice DA, Chen X. *In vitro* and *in vivo* characterization of ^{64}Cu-labeled Abegrin™, a humanized monoclonal antibody against integrin $\alpha_v\beta_3$. *Cancer Res.* 2006;66:9673–9681.
26. Meares CF, McCall MJ, Reardan DT, Goodwin DA, Diamanti CI, McTigue M. Conjugation of antibodies with bifunctional chelating agents: isothiocyanate and bromoacetamide reagents, methods of analysis, and subsequent addition of metal ions. *Anal Biochem.* 1984;142:68–78.
27. Chen X, Conti PS, Moats RA. *In vivo* near-infrared fluorescence imaging of integrin $\alpha_v\beta_3$ in brain tumor xenografts. *Cancer Res.* 2004;64:8009–8014.
28. Cai W, Shin DW, Chen K, et al. Peptide-labeled near-infrared quantum dots for imaging tumor vasculature in living subjects. *Nano Lett.* 2006;6:669–676.
29. Zhang X, Xiong Z, Wu X, et al. Quantitative PET imaging of tumor integrin $\alpha_v\beta_3$ expression with ^{18}F-FRGD2. *J Nucl Med.* 2006;47:113–121.
30. Chen X, Plasencia C, Hou Y, Neamati N. Synthesis and biological evaluation of dimeric RGD peptide-paclitaxel conjugate as a model for integrin-targeted drug delivery. *J Med Chem.* 2005;48:1098–1106.
31. Xiong Z, Cheng Z, Zhang X, et al. Imaging chemically modified adenovirus for targeting tumors expressing integrin $\alpha_v\beta_3$ in living mice with mutant herpes simplex virus type 1 thymidine kinase PET reporter gene. *J Nucl Med.* 2006;47:130–139.
32. Chen X, Sievers E, Hou Y, et al. Integrin $\alpha_v\beta_3$-targeted imaging of lung cancer. *Neoplasia.* 2005;7:271–279.
33. Sgouros G. Dosimetry of internal emitters. *J Nucl Med.* 2005;46(suppl 1):18S–27S.
34. Folkman J. Tumor angiogenesis: therapeutic implications. *N Engl J Med.* 1971;285:1182–1186.
35. El-Mousawi M, Tchistiakova L, Yurchenko L, et al. A vascular endothelial growth factor high affinity receptor 1-specific peptide with antiangiogenic activity identified using a phage display peptide library. *J Biol Chem.* 2003;278:46681–46691.
36. Goncalves M, Estieu-Gionnet K, Berthelot T, et al. Design, synthesis, and evaluation of original carriers for targeting vascular endothelial growth factor receptor interactions. *Pharm Res.* 2005;22:1411–1421.
37. Guo J, Higashi K, Ueda Y, et al. Microvessel density: correlation with ^{18}F-FDG uptake and prognostic impact in lung adenocarcinomas. *J Nucl Med.* 2006;47:419–425.